



1

<sup>2</sup> **Supplementary Information for**  
<sup>3</sup> **Clocked Atom Delivery to a Photonic Crystal Waveguide**  
<sup>4</sup> **A. P. Burgers, L. S. Peng, J. A. Muniz, A. C. McClung, M. J. Martin, and H. J. Kimble**  
<sup>5</sup> **Corresponding Author Name.**  
<sup>6</sup> **E-mail:** hjkimble@caltech.edu

<sup>7</sup> **This PDF file includes:**  
<sup>8</sup>      Supplementary text  
<sup>9</sup>      Figs. S1 to S8  
<sup>10</sup>     Captions for Movies S1 to S2  
<sup>11</sup>     References for SI reference citations

<sup>12</sup> **Other supplementary materials for this manuscript include the following:**  
<sup>13</sup>     Movies S1 to S2

14 **Supporting Information Text**

15 **Experimental Set-up**

16 The experimental process starts by pushing, with a near resonant pulsed beam, a continuously loaded MOT in the source  
17 chamber down a differential pumping tube to the science chamber (1). The pushed atoms are recaptured in the science chamber  
18 MOT where we load them into a 1D lattice from two counter-propagating beams originated from the same titanium sapphire  
19 (Tisapph) laser,  $B_1$  and  $B_2$ . Both beams are passed through acousto-optic modulators (AOMs) to control the relative frequency  
20 between them, the intensity, and to achieve fast switching times. The 1D lattice loads from atoms in the science MOT by  
21 way of an interval of polarization gradient cooling (PGC), which is followed by a degenerate Raman sideband cooling (DRSC)  
22 interval to achieve a final axial temperature of  $12 \mu\text{K}$  (1).

23 Once the atomic sample has been loaded and cooled, one of the AOMs is frequency chirped from the normal operation at  
24 80 MHz to 81.2 MHz (for the case of the experimental data presented, however, as stated in the manuscript, the final chirp  
25 difference frequency can be arbitrarily defined). This chirp sequence is achieved by utilizing a signal generator set to 70 MHz  
26 and mixing with a 10MHz signal from a programmable direct digital synthesizer (DDS)(Analog Devices AD8954). A tunable  
27 filter is used to block the lower frequency component from mixing. The chirping sequence is written to the DDS memory using  
28 an ‘Arduino DUE’ microcontroller. The chirping sequence ramps the frequency from 10MHz to the desired RF frequency (here  
29 11.2 MHz to achieve a 1.2MHz beat and a lattice speed of 0.51 m/s), thereby creating a moving optical lattice. The atoms are  
30 conveyed over a distance of 20 mm to the center region of a particular APCW device via the moving 1D optical lattice (i.e.,  
31 ‘optical conveyor belt’) with temperature in the moving lattice frame (typically  $\sim 10 - 30 \mu\text{K}$ ) much less than the lattice depth  
32 (typically  $\sim 300 - 500 \mu\text{K}$ ).

33 As the confined atomic cloud passes a chosen APCW, atoms near the waveguide are interrogated by a weak guided-mode  
34 (GM) probe injected into the APCW with frequency  $\omega_p$  tuned around the atomic free-space resonance  $\omega_a$ . The transmitted  
35 probe beam is separated spectrally from lattice light that scatters into the APCW by a volume Bragg grating (VBG), as well  
36 as from light in any other (GMs), which are used in some experiments. The transmitted and reflected probe light is detected  
37 by single-photon counting modules (SPCMs) with a time stamp recorded for each detected photon. Scattered lattice light that  
38 emerges in a GM is likewise detected, both by a SPCM, as well as an analog APD to produce time-stamps and a real-time  
39 zero crossing signal, respectively, which is likewise recorded to fix sequential lattice periods. The lattice time tags and the  
40 probe time tags are registered to each other and a ‘clocked’ histogram created for a single lattice period as described in the  
41 manuscript (Fig. 3).

42 One experimental concern is determining the relative phase between the atomic signature and the lattice sync signal. Due  
43 to the (assumed) random distribution of scatterers on the surfaces of the waveguide, the time of largest scattering into the  
44 waveguide can vary relative to the time of maximum intensity centered in the gap of the APCW (i.e., what we define as  $t = 0$   
45 for the simulated clocked spectra). Since the thickness of the device is 200 nm with a refractive index  $n_{SiN} = 2$ , the optical  
46 distance is 400 nm, which is comparable to the distance between adjacent pancakes ( $\simeq 425$  nm) in free-space. This can cause a  
47 shift in the clocked spectrum by roughly half the lattice period  $\pm\tau_{lattice}/2$  depending on the distribution of scatterers for each  
48 different device surface. We have modeled such processes by calculations of the field intensity of the moving lattice in various  
49 regions of the APCW (e.g., 10 nm depth of the front or back surface, and the inner and outer walls) and numerically found  
50 offsets  $\simeq \pm\tau_{lattice}/2$ . Furthermore, the scattered power into the waveguide from each individual lattice beams  $B_1$  (incident on  
51 the front surface) and  $B_2$  (incident on the back surface) is generally not equal, though the powers are the same in free-space,  
52 where this ratio varies from device to device. This supports the supposition that scattering of lattice light into GMs arises from  
53 fabrication-dependent defects and not systematic imperfections.

54 Operationally, we use two methods to correct the measured clock spectra to account for time offsets between the lattice  
55 sync signal and the ‘true’ time for which lattice maxima from successive lattice periods cross the center line of the APCW  
56 along  $z$ . First of all, we employ a method for which a clocked spectrum with no GM Stark beam is summed over all detunings  
57  $\Delta_p$  for a given laboratory offset time (i.e., project a clocked spectrum onto the time axis). The minimum optical depth in time  
58 is then offset in time to correspond to clocked time  $t = 0$ . A second method utilizes a cross-correlation technique between the  
59 probe counts at a single detuning and the lattice fringe signal by offsetting the relative timing in such a way that the highest  
60 correlation point is at lattice time  $t = 0$ . Both these methods agree within the  $\simeq 50$  ns uncertainty of our timing logic for the  
61 lattice sync signal.

62 We emphasize that the offset found for a given device determined by these techniques is constant but varies from device to  
63 device over the expected range  $\simeq \tau_{lattice}/2$ . For more detailed comparisons between a set of measured and simulated spectra as  
64 displayed in Fig. 4, we allow a small additional offset for the data set as a whole.

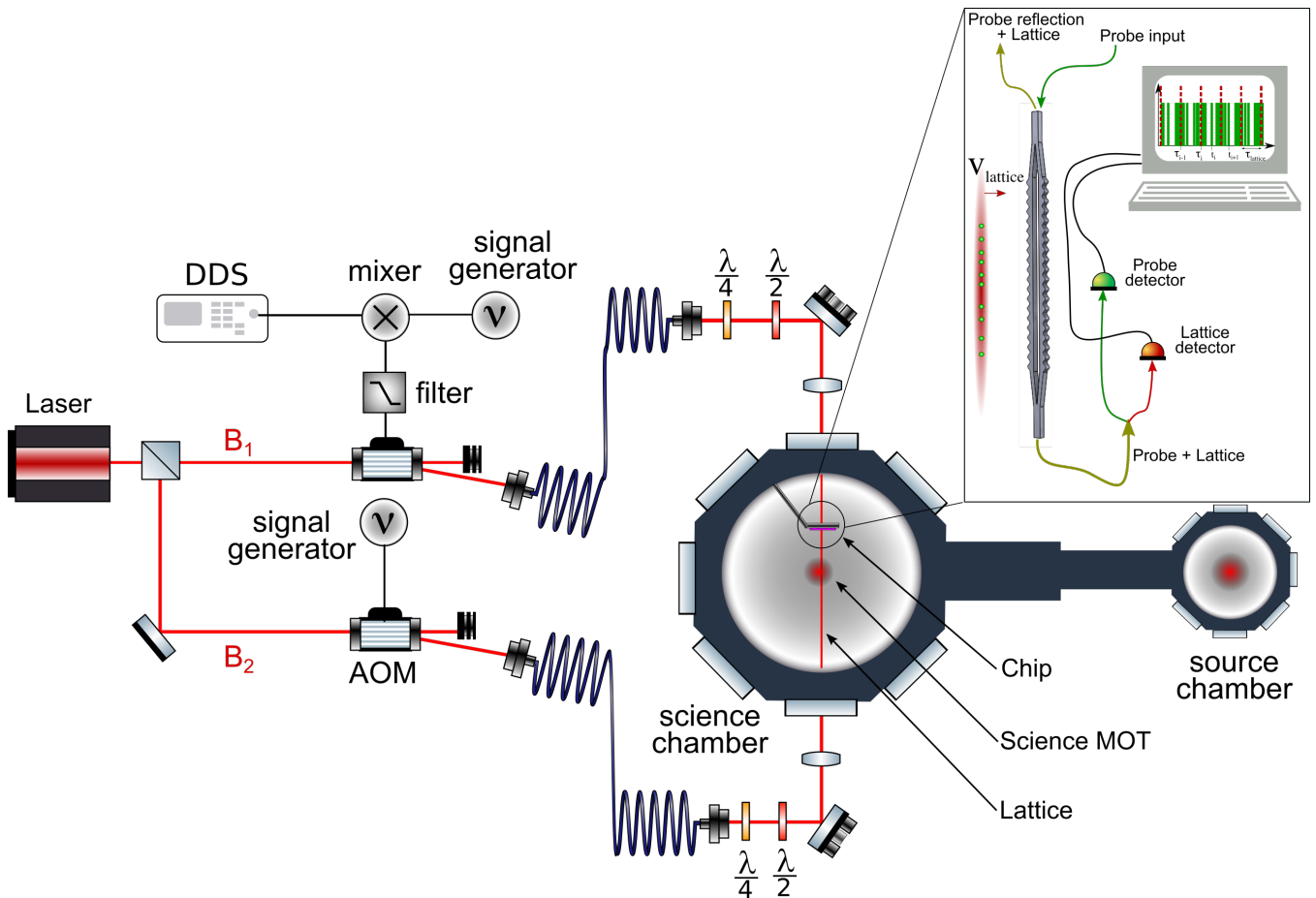


**Fig. S1.** Schematic of the experimental apparatus. The Science chamber is loaded by pushing a source MOT from the Source chamber through a differential pumping tube to the Science chamber. The 1D optical lattice (conveyor belt) originates from a Ti:sapph laser and is split sending each beam,  $B_1$  and  $B_2$ , to an acousto-optic modulator (AOM). One of the AOMs receives a frequency chirp sequence from a direct digital synthesizer (DDS) creating a moving optical lattice that conveys the atoms to a particular APCW on a chip with multiple such devices. (Inset) The atoms interact with the waveguide through GMs of the structure, in particular a weak probe tuned around the atomic free-space resonance. The probe light and lattice light are separated by Volume Bragg Gratings (VBGs) and each detected and digitized to create the histograms presented in the manuscript.

65 **Fitting  $\Gamma_{1D}^{\text{eff}}$  and  $J_{1D}^{\text{eff}}$  from Clocked Data**

66 We fit the measured ‘clocked’ spectra to a transmission model of the probe field through the PCW that was developed in (2, 3),  
 67 which is expressed as follows:

$$T(\Delta_p, t) = \left| \frac{\Delta_p + i\Gamma'/2}{(\Delta_p + J_{1D}^{\text{eff}}(t)) + i(\Gamma' + \Gamma_{1D}^{\text{eff}}(t))/2} \right|^2. \quad [1]$$

Here  $\Delta_p$  is the detuning between the probe frequency and the free-space atomic resonance frequency,  $\Gamma'$  is the atomic decay rate into all modes (mostly free-space) other than the GM of interest, and  $\Gamma_{1D}^{\text{eff}}(t)$  and  $J_{1D}^{\text{eff}}(t)$  are the emission rate into the waveguide and the atom-atom coupling rate for the GM of interest, respectively. The time dependence of  $\Gamma_{1D}^{\text{eff}}$  and  $J_{1D}^{\text{eff}}$  arises from the periodic arrival and transit of the atoms. For the ideal case of a single lattice ‘pancake’ with atomic and probe frequencies near the band edges of the APCW, we would find that

$$\Gamma_{1D}^{\text{eff}}(t) = \sum_{i=1}^{N_{\text{at}}} \Gamma_{1D}^{ii}(r_i(t)), \quad [2]$$

68 where  $N_{\text{at}}$  is the number of atoms within a single pancake and  $r_i$  is the position of the  $i^{\text{th}}$  atom.

69 However, in our experiment it is difficult to disentangle the number of atoms interacting with the waveguide and the spatial  
 70 variation of  $\Gamma_{1D}$  for different atoms and trajectories. Hence, we introduce  $\Gamma_{1D}^{\text{eff}}$  as an effective atomic coupling to the waveguide,  
 71 and likewise for the term  $J_{1D}^{\text{eff}}$ , which was found to be quantitatively adequate for the analyses in (2). In microscopic terms,  
 72  $J_{1D}^{ij}$  and  $\Gamma_{1D}^{ij}$  relate to the real and imaginary components of the Green’s function for radiative interactions between atoms  
 73 ( $i, j$ ), mediated by the GM of interest of the APCW.

74 From the effective model of Eq. 1, the coupling strengths  $\Gamma_{1D}^{\text{eff}}(t)$  and  $J_{1D}^{\text{eff}}(t)$  can be extracted as functions of the clocked  
 75 lattice time by taking detuning cuts of the 2D spectrum at fixed times in Fig. 3(e) and fitting each spectrum to the above  
 76 model. An example of measurements at one time slice and the corresponding fit of the spectrum is shown in Fig. 3(f). Such  
 77 fits can be performed for each time  $t$  in a 2D clocked spectrum to extract the temporal behavior of the fit parameters versus  
 78  $t$  and thereby obtain further information about atomic couplings to the waveguide on a microscopic scale as the successive  
 79 lattice periods of atoms move through the device.

80 **Clocked Spectra with Different GMs**

81 Here we present additional experiment and simulation results. Fig. S2 shows the measured and simulated spectra for a  
 82 blue-detuned TM Stark GM with a weak TE probe. The polarization and frequency configuration of the involved beams is  
 83 presented in Fig. S3. Evident in this figure is that the agreement between simulation and experiment, while still good, is not  
 84 quite so good compared to Fig. 4 in the main text. We suspect this is due to the usage of TE GMs for probing, which have a  
 85 complicated modulation pattern in the  $x$  direction that is not addressed in the current 2D simulations (2). We are working  
 86 towards implementing 3D simulations to better characterize the trajectories in the presence of the full APCW. This TE probe  
 87 configuration is utilized to gain sensitivity to the atomic trajectories that enter into the APCW vacuum gap, as indicated in  
 88 Fig. 6 from the main text. From Fig. 6 in the main text, vacuum gap atoms appear separated from the other trajectories (‘side’  
 89 and ‘others’) in detuning at  $\simeq 160$  ns. The clocked spectra in Fig. S2, provide preliminary evidence for the atoms entering the  
 90 vacuum gap, which is essential for loading any FORT within the APCW.

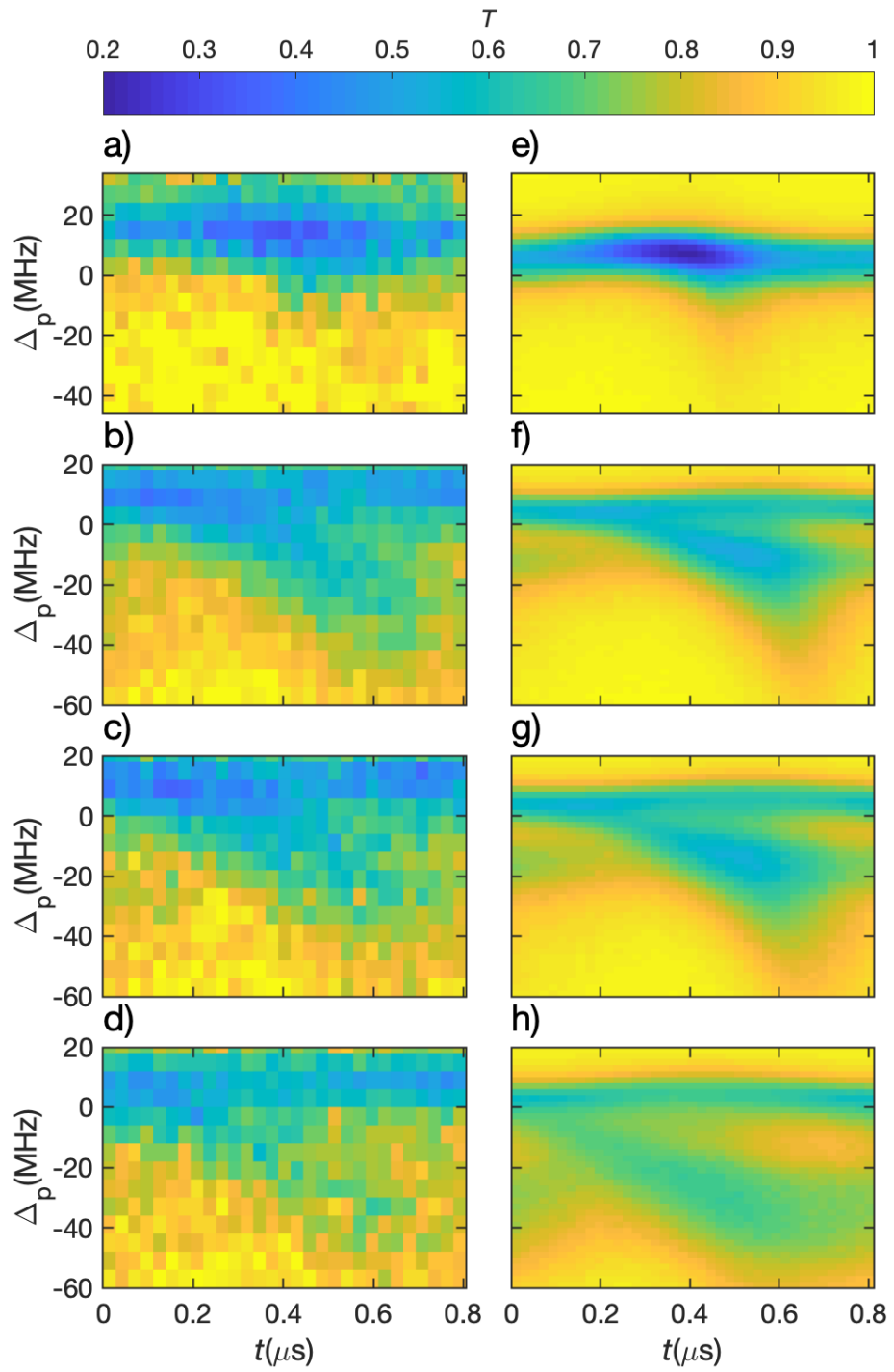


**Fig. S2.** A comparison of data (a-d) and simulation (e-h). A blue detuned TM Stark GM is excited in the APCW, and the atoms are probed with a weak TE probe with detuning  $\Delta_p$ . The polarization and frequency configuration of the involved beams is presented in Fig. S3. For the measurements in the left column of the Figure, the sequence of input powers is  $P_{\text{Stark}} = \{0, 20, 30, 52\} \mu\text{W}$  from top to bottom. For the simulations in the right column, from top to bottom, the internal power sequence is  $P_{\text{Stark}} = \{0, 3.7, 5.6, 9.7\} \mu\text{W}$  for the GM detuning of 58 GHz from  $F = 3$  on the D2 line.

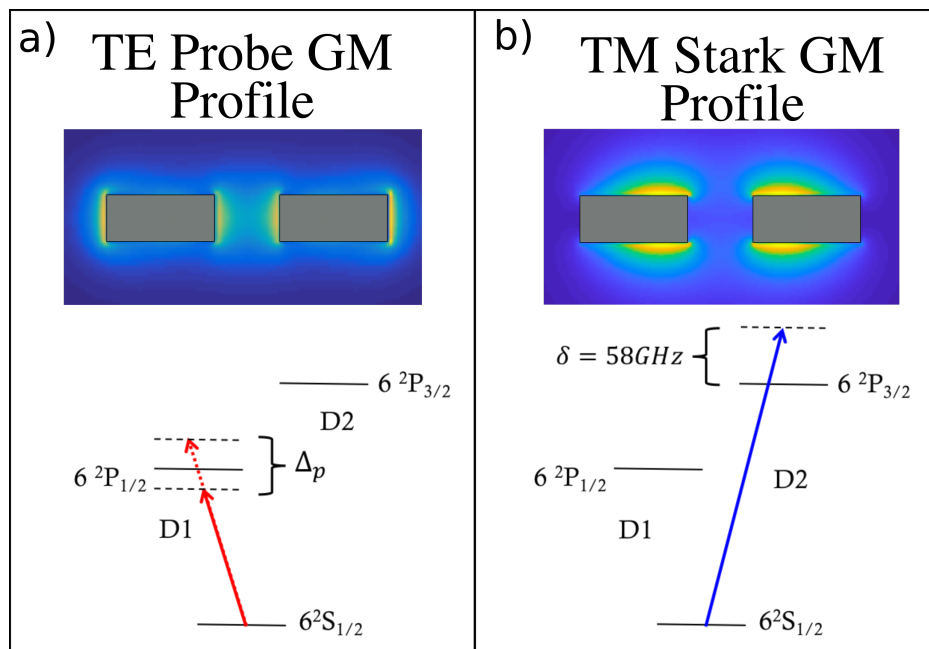


**Fig. S3.** The beam frequency and polarization parameters for the data in Fig. S2, Fig. 6 of the main text and Fig. 3e of the main text, albeit without the TM Stark GM. a) The TE probe GM spatial profile. Below shows the frequency detuning of the probe beam which is scanned around the free-space D1 resonance. b) The TM Stark GM profile with the detuning from the D2 line. The detuning is held fixed for all measurements at 58MHz

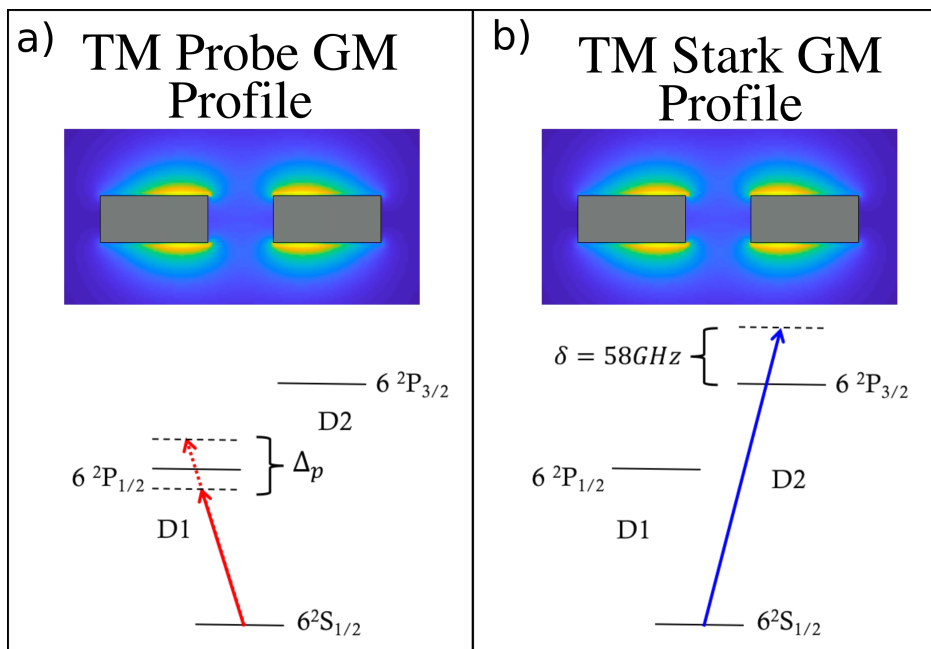


**Fig. S4.** The beam frequency and polarization parameters for the data in Fig. 4, Fig. 5(b)(c)(e)(f) and Fig. 7 of the main text. a) The TM probe GM spatial profile. Below shows the frequency detuning of the probe beam which is scanned around the free-space D1 resonance. b) The TM Stark GM profile with the detuning from the D2 line. The detuning is held fixed for all measurements at 58MHz

91 **Simulations**

92 Here we present the details of the numerical simulations of atom trajectories and APCW transmission spectra. First, 2D atom  
 93 trajectories ( $y(t), z(t)$ ) are calculated by solving the equations of motion of atoms in optical dipole and Casimir-Polder (CP)  
 94 potentials. Then, the atom trajectories are sampled and distributed along the  $x$  direction with the probability distribution of  
 95  $P(x)$ , depending on the probe intensity profile (i.e., TE or TM mode). The APCW transmission spectra can be calculated  
 96 with the transfer matrix model by representing ‘distributed’ atom  $i$  at position  $(x_i(t), y_i(t), z_i(t))$  and the waveguide segment  
 97 between atoms with transfer matrices. The simulation process is summarized in the flowchart in Fig. S5.

98 The simulations for atomic transport are carried out in the 2D-space of  $y, z$  to reduce the required computational resources  
 99 and enable more rapid explorations of parameter space. Justification for this reduction from full 3D is that the lattice fields  
 100 along  $x$  for full 3D simulations exhibit only small modulation ( $\lesssim 5\%$ ), as is also the case for so-called side-illumination (SI)  
 101 traps employed in Refs.(2, 4). Full simulations in 3D are currently in development. For the 2D simulations in this work, the  
 102 center gap of the APCW is located at the origin, the simulation domain extends  $\pm 25 \mu\text{m}$  along  $y$  and from  $-10 \mu\text{m}$  to  $60 \mu\text{m}$   
 103 along  $z$  in a plane that contains the thick part of the APCW, with atoms initialized at  $z \simeq 60 \mu\text{K}$  moving toward  $-z$  direction.

104 The total potential  $U(t)$  for an assumed independent atom consists of three contributions: 1). The optical lattice,  $U_{\text{lattice}}(t)$ ,  
 105 which differs significantly from free-space due to forward and backward scattering from each, otherwise independent, counter-  
 106 propagating lattice beam off the APCW. Here  $U_{\text{lattice}}(t)$  is calculated using the finite element method (FEM) implemented  
 107 in COMSOL (5). 2). GM fields,  $U_{\text{GM}}(t)$ , input to the APCW, where  $U_{\text{GM}}(t)$  is determined from eigenmode calculations  
 108 for the APCW GMs done with MPB (6). 3). Finally, the CP potential,  $U_{\text{CP}}$ , originating from the interaction between  
 109 the atoms and the dielectric surfaces (7). Potentials 1) and 2) are the ground-state optical dipole potential, which can  
 110 be calculated from the field intensity (8). Atoms are initialized in  $U_{\text{lattice}}$  with a Boltzmann distribution for temperatures  
 111 ranging over  $10 \mu\text{K} < T_{\text{initial}} < 150 \mu\text{K}$  and for lattice depths  $200 \mu\text{K} < U_{\text{lattice}}^{\text{initial}} < 500 \mu\text{K}$  at a distance  $60 \mu\text{m}$  from the  
 112 APCW in  $z$ , where the scattered fields from the APCW are small. Atomic trajectories are calculated by solving the classical  
 113 equations of motion with SUNDIAL differential equation solver (9) for the assumed independent atoms in the potential  
 114  $U(r, t) = U_{\text{lattice}}(r, t) + U_{\text{GM}}(r) + U_{\text{CP}}(r)$ . For the current parameters for our experiments, the nonadditive corrections of  
 115 optical potential and CP potential (10, 11) is estimated to be small for all the beams involved.

116 **Transfer Matrix Model.** To calculate the APCW transmission spectrum as a function of time, the atom trajectories are randomly  
 117 sampled according to the experimentally measured density of  $\simeq 500$  atoms per pancake. The sampled atom trajectories are  
 118 then distributed along the  $x$  direction with probability proportional to the probe intensity in the APCW, as shown in Fig.  
 119 S6. For example, for a TE probe with frequency near the APCW TE band edge, the atom trajectories are distributed with  
 120 a  $\cos^2(2\pi x/a)$  probability distribution, where  $a$  is the APCW unit cell spacing (370 nm), to approximate the high contrast  
 121 TE Bloch mode. For a TM probe with frequency near the Cs D1 or D2 transitions, the TM band edges are both far from  
 122 the probe frequency (2) with low contrast Bloch modes (i.e., effectively traveling waves), so that the atom trajectories are  
 123 distributed uniformly along  $x$ . Since our GM probe field is far below saturation, the transmission of the system as a function of  
 124 probe frequency can be calculated with the transfer matrix model (2, 3, 12).

125 Light propagation along the APCW and atoms system can be modeled with the transfer matrix model. For a probe with  
 126 detuning  $\Delta$  relative to shifted ground-state and excited-state transition frequency, the transfer matrix of an atom is:

$$128 M^{\text{atom}}(\Delta_p, \Gamma_{1\text{D}}, \Gamma') = \begin{pmatrix} t - \frac{r^2}{t} & \frac{r}{t} \\ -\frac{r}{t} & \frac{1}{t} \end{pmatrix} \quad [3]$$

129 where  $r = -\frac{\Gamma_{1\text{D}}}{\Gamma_{1\text{D}} + \Gamma' - i2\Delta_p}$  and  $t = 1 + r$  (12).

130 And for a waveguide of length  $l$  and angular wavenumber  $k$ ,

$$131 M^{\text{wg}}(k, l) = \begin{pmatrix} e^{ikl} & 0 \\ 0 & e^{-ikl} \end{pmatrix} \quad [4]$$

132 With the atom trajectories distributed along the  $x$  direction ( $x(t), y(t), z(t)$ ). To calculate the transmission at time  $t$ , the  $i^{\text{th}}$   
 133 atom can be modeled with the transfer matrix  $M_i^{\text{atom}}(\Delta, \Gamma_{1\text{D}}, \Gamma')$  in Eq. 3, with the detuning  $\Delta_p$  calculated from ground-state  
 134 and excited-state light-shifts induced by the lattice, GM and CP potential. The emission rate into the waveguide  $\Gamma_{1\text{D}}$  is  
 135 proportional to the probe intensity profile, and  $\Gamma'$  is the decay rate into free-space and other GMs. The waveguide segment  $i$   
 136 between atom  $i-1$  and atom  $i$ , can be modeled with eqn. 4. The total transfer matrix  $M^{\text{tot}}$  is the product of all transfer  
 137 matrices along the waveguide,  $M^{\text{tot}} = \prod_{i=1}^n (M_i^{\text{wg}} \times M_i^{\text{atom}})$ , where  $n$  is the number of the sampled atoms, as shown in Fig. S6.  
 138 The transmission of the APCW and atoms system can then be extract from the total transfer matrix  $M^{\text{tot}}$ .

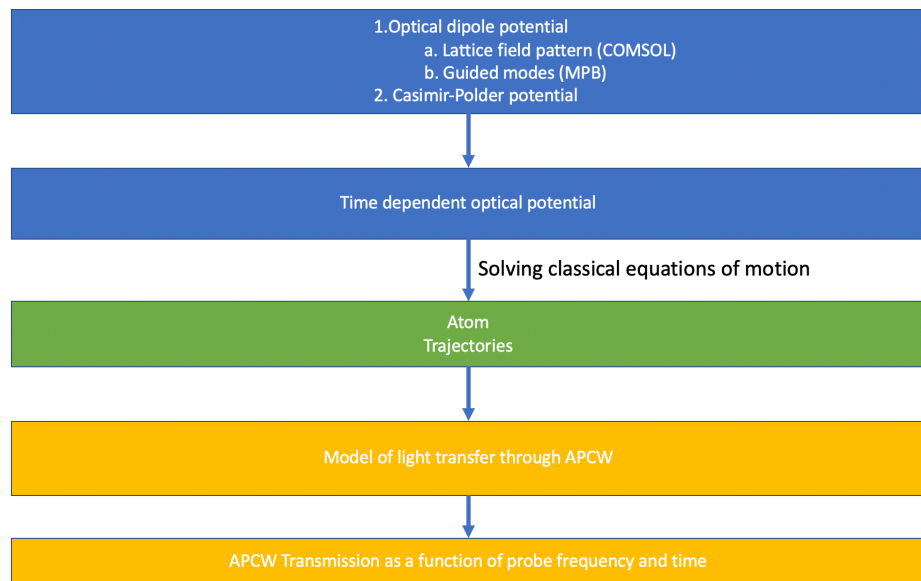


**Fig. S5.** The flowchart of the numerical simulation. First, the optical dipole potentials and the CP potential are calculated and combined to form the time-dependent potential. Then, atoms are initialized into the optical potential far from the APCW and the equations of motion are solved to generate the atom trajectories. The transmission  $T(\Delta_p, t)$  as a function of probe detuning and time is then calculated with the transfer matrix model.

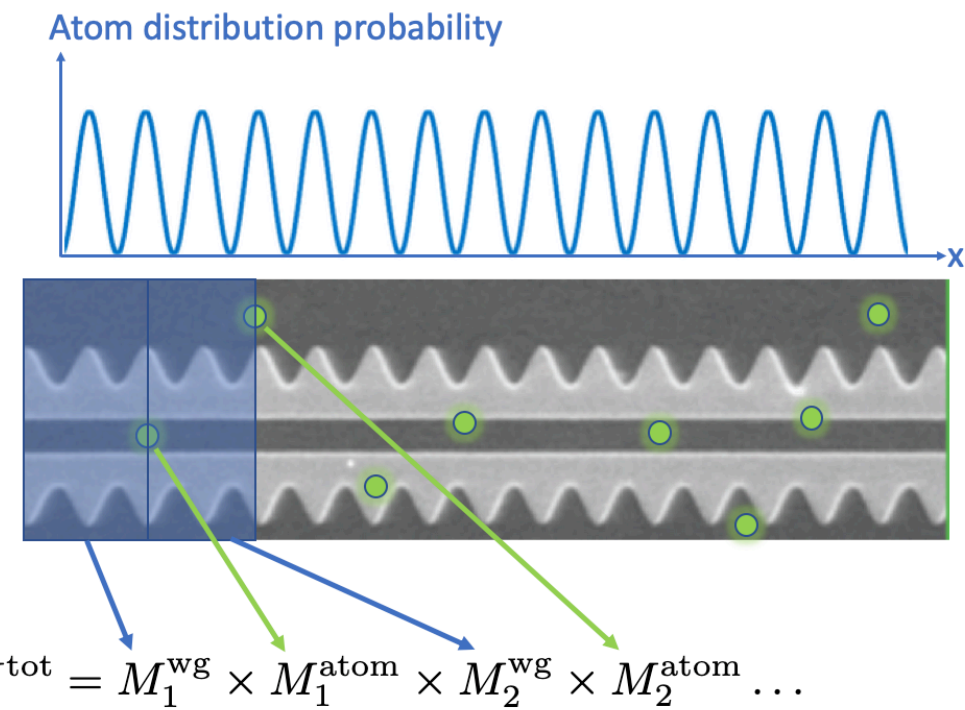


**Fig. S6.** Diagrammatic look at the transfer matrix model. For a TE probe simulation, atoms are distributed along the APCW in the  $x$  direction weighted by the sinusoidal intensity distribution of a GM at the TE dielectric band edge. Light propagation along the APCW is modeled with the transfer matrix model. Each atom and the waveguide segments between adjacent pairs of atoms are represented with a transfer matrix, with the total transfer matrix being the product of all transfer matrices. The transmission of the whole system can be extract from the total transfer matrix.

139 **Surface Forces**

140 Experiments measuring the influence of surface forces on BECs have shown that alkali atoms adsorbed on the surfaces can  
141 produce strong electric fields creating potentials larger than the traditional CP potential (10, 13). The following is a discussion  
142 of how this might affect our system and provide some preliminary indications that such forces are likely not present in our  
143 system.

144 At our current (rather poor) level of accuracy between experiment and simulation, we find no indication that additional  
145 surface forces are relevant besides CP. If such forces were to exist in our system with strengths similar to CP then atom  
146 trapping would still be possible only the guided mode trap potentials would need to be altered to accommodate the extra  
147 potential. If, however, these forces were much larger (order of magnitude) than CP then we would no longer be able to deliver  
148 a GM sufficient to cancel the new potential due to the power handling limitations of our current devices. A new generation of  
149 devices has been fabricated and is being evaluated that should allow 20 $\times$  higher powers for GM traps.

150 As for possible mechanisms for additional surface potentials beyond CP, we have devoted considerable effort to understanding  
151 the deposition of Cs on our structures. We are able to measure shifts in our bandstructure due to Cs deposition to 1 part in 10<sup>5</sup>,  
152 which has allowed us to compare to theoretical models of the index of refraction of the material deposited on the waveguide.  
153 For the case of Cs metal deposition with a permittivity  $\epsilon_{\text{Cs}} = -3.8 + 1.2i$ , our models (that assume a conformal coating) predict  
154 that the dielectric bandedge shifts to higher frequency with increasing mass deposited. However, if a dielectric coating is being  
155 deposited on the structure (for example Cs<sub>2</sub>O with a permittivity  $\epsilon_{\text{Cs}_2\text{O}} = 4.8 + 0.8i$ ), our models predict that the dielectric  
156 bandedge would shift to lower frequency with increased deposition. Experimentally, we observe that in measurements such as  
157 reported in our manuscript, the bandedge shifts to lower frequency without exception, which is consistent with a dielectric  
158 coating on the structure (of thickness ~5-10 nm).

159 Spurred by the referee's comments, we have further reviewed the literature investigating atom-surface interactions as it  
160 relates to patches of deposited alkali atoms. Ref. (14) discusses the interaction of BECs with surface forces and the role of  
161 alkali atoms deposited on the surface of metals which could influence these interactions. It appears that this effect is largely due  
162 to the comparable work function of the metal and the ionization energy of the atom creating a localized dipole at the surface.  
163 The electric field gradient from the dipole creates a spatially dependent force on the BEC to which such experiments are quite  
164 sensitive. Again, in our experiment the deposition is on a dielectric surface (Silicon Nitride) and not a metal. Furthermore, our  
165 measurements of the bandedge shift is consistent with a conformal deposition of an insulator so no surface dipoles should be  
166 present. In fact, Ref. (14) discuss the case where atoms are adsorbed on glass and determine the electric field gradient. The  
167 effects are stated to be negligible for atoms on glass (albeit at distance scales much larger than in our work), which is the  
168 closest analogue to our Silicon Nitride waveguides. Such experiments with BECs are carried out by observations of changes in  
169 trap frequency of the BEC and are as such highly sensitive to changes in the environment. In contrast, we do not yet have  
170 trapped atoms so our measurements are currently far from the accuracy regime of those mentioned above. We believe that  
171 achieving trapped atoms will help us to make more precise measurements of the surface forces through trap frequency shifts  
172 and allow us to definitively answer this important question. Unless of course these additional surface forces are so large as to  
173 preclude trapping.

174 Currently, we are developing techniques for measuring the mass loading on our waveguides using the mechanical vibration  
175 spectrum. These devices exhibit mechanical Q's of  $\sim 2 \times 10^5$  at  $\sim 2.3$  MHz so we are optimistic that measurements of the  
176 mechanical frequency shift can shed some light on the mechanism of Cs loading on to the waveguide.

177 **Guided Mode Traps**

178 The GMs of the alligator photonic crystal waveguide (APCW) can be utilized to create stable trapping potentials in the  
179 vacuum gap between the dielectric beams (15, 16). GMs at each band edge exhibit a periodic structure within the APCW as  
180 seen in Fig. S7.

181 A two color trap utilizes the periodic structure of the APCW by tuning one GM to a higher frequency (58 GHz) than the  
182 free-space atomic resonance so that the dipole force repels the atoms from this band edge. The second GM is tuned to a  
183 frequency lower than the atomic resonance (600 GHz) creating an attractive potential. Though these dipole force GMs are at  
184 different wavelengths, the Bloch modes of the structure set the scale for the trap locations. The result of this two-color trap  
185 scheme leads to the trapping potentials shown in Fig. S7.

186 For the data presented in our manuscript, atoms are traveling at 0.51 m/s through these trapping potentials, transiting  
187 the roughly 100 nm trap size in only 200 ns. To achieve trapping, the atoms must cool and trap in times shorter than  
188 traditional mechanisms for laser cooling and trapping of atoms. Hence we must incorporate a faster trapping scheme, here  
189 based upon that utilized in Ref. (17). The atoms arrive in one of the ground state manifolds, say  $F = 4$ , and enter the trap  
190 region. The trap is configured in such a way that the trap surface for  $F = 4$  is shallow compared to  $F = 3$ , so that the atoms  
191 pick up little additional kinetic energy as they move down into the trap. When the atoms are near the trap center an optical  
192 pumping pulse promotes population to an electronic excited state where it decays with roughly equal probability to  $F = 3$  or  
193  $F = 4$ . Atoms decaying to  $F = 4$  will simply continue their motion and 'roll' out of the conservative potential; however, atoms  
194 decaying to  $F = 3$  will retain approximately the same kinetic energy only now on the different trap surface for  $F = 3$ . The  
195 kinetic energy of the atoms is now insufficient to overcome the trap potential for  $F = 3$  and the atoms are now trapped. A  
196 schematic of this process is provided in Fig. S8. In the trapping scheme described above, triggering the optical pumping pulse  
197 to initiate the state transfer must be done at a specific time to ensure the atoms are transferred to near the minimum of the  
198  $F = 3$  surface. Clocked delivery provides important information about when the atoms are arriving into the center of the

199 APCW, but perhaps more importantly, the clocked signal provides us with a trigger for the optical pumping pulse. This is  
200 another useful advantage to utilizing the clocked delivery method we describe in the manuscript.

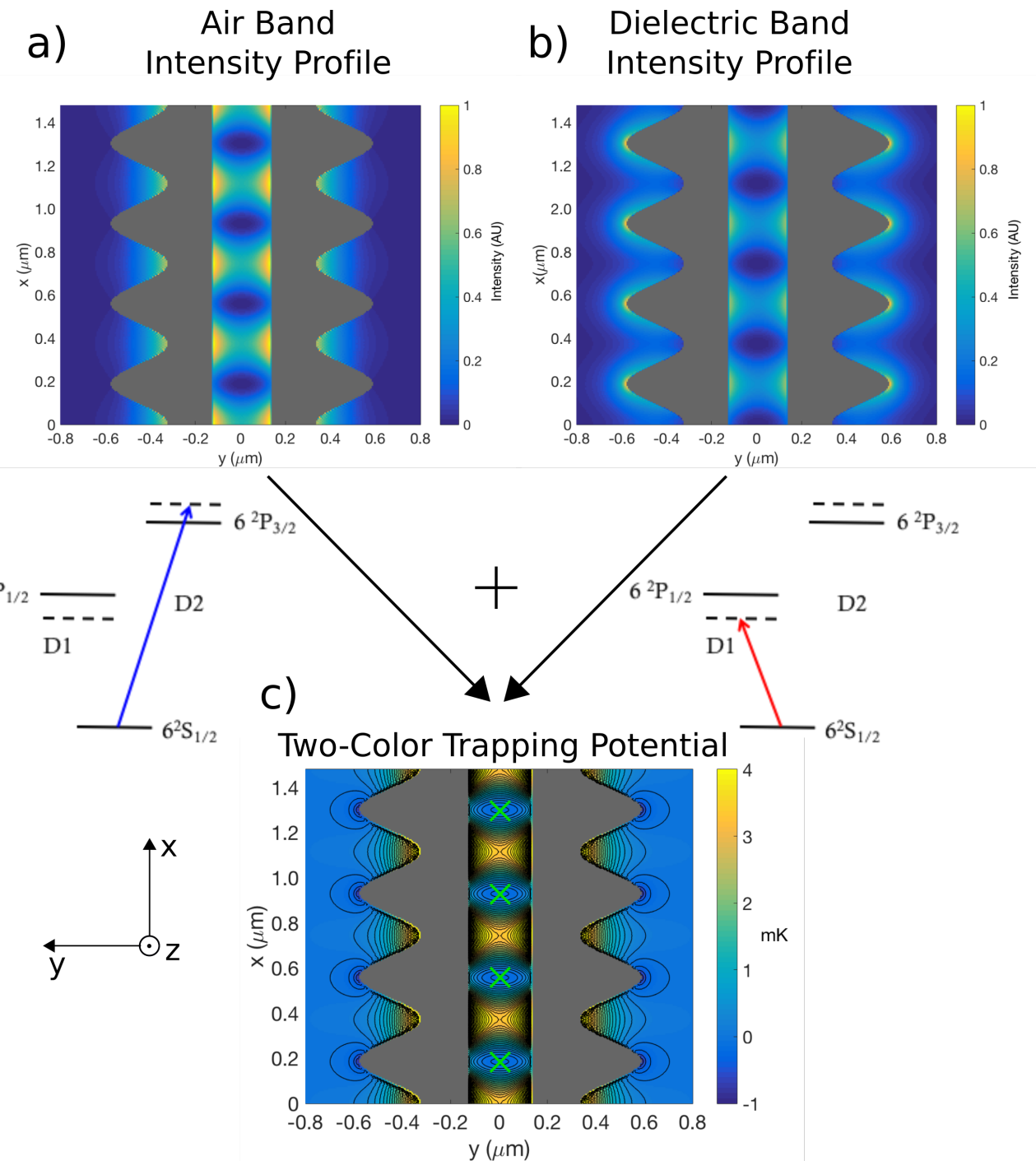


**Fig. S7.** Stable trap sites within the alligator photonic crystal waveguide (APCW) created using blue and red detuned beams at the air bandedge and dielectric bandedge (15, 16). a) By way of a repulsive optical dipole force, atoms are kept off the walls of the structure. b) An attractive optical dipole force creates a periodic trapping potential along the length ( $x$  direction) of the waveguide. This red detuned trap light also creates an attractive potential primarily utilized to create confinement out of the page ( $z$  direction). c) Total optical trap with the green 'X's indicating stable trapping points.

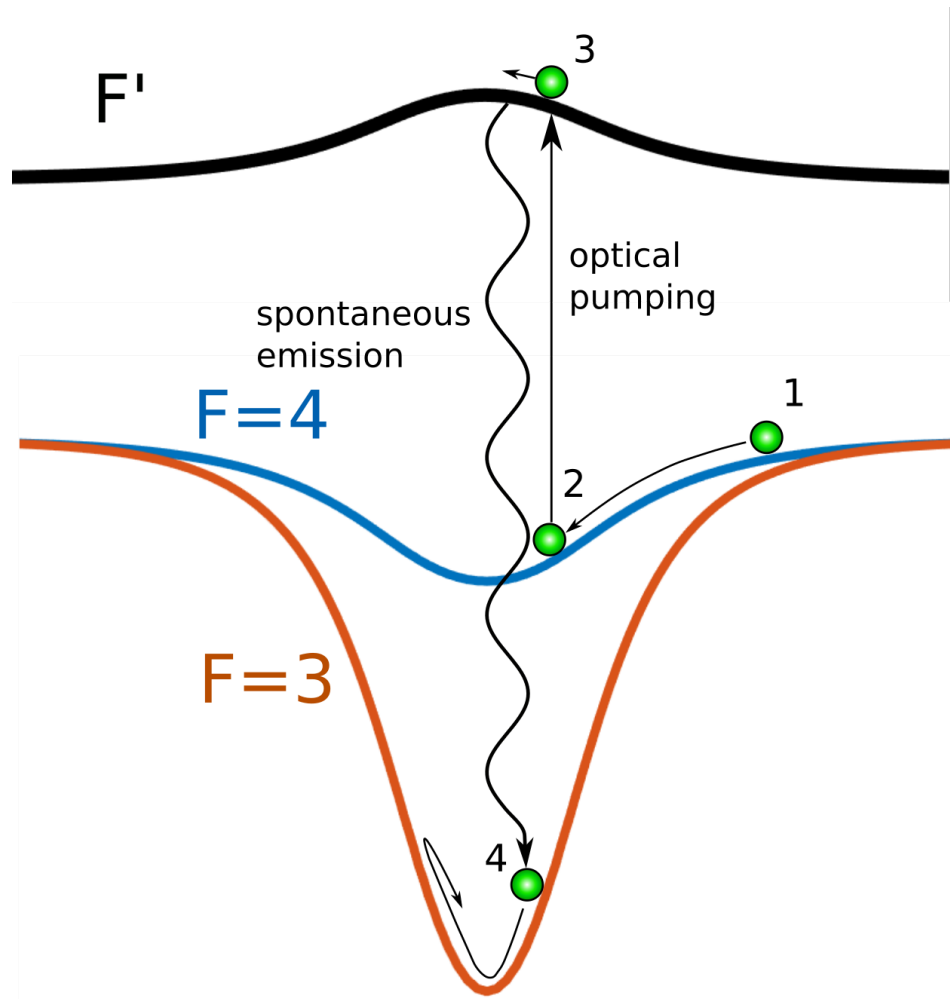


**Fig. S8.** A schematic of the implementation of the scheme in Ref. (17) here illustrated for a cross-section of the GM trap. Atoms arrive into the trap within the APCW structure in  $F = 4$  and accelerate down the  $F = 4$  potential (point 1). When the atom is near the center of a unit cell of the APCW, an optical pumping pulse is triggered exciting the atom to a higher electronic  $F'$  state (point 2). The atom is in the excited state for a short time before decaying through spontaneous emission (point 3). If the atom decays to  $F = 3$  it retains approximately the same kinetic energy but now the potential barrier around it is larger than the atom's kinetic energy (point 4). The atom is thus trapped on the  $F = 3$  trap surface.

201 **Simulation Movies**

202 The following movies present two cases of simulated trajectories for no TM Stark GM (Movie S1) and including a TM Stark  
203 GM (Movie S2). The potentials present in the simulation are determined by the free-space conveyor belt lattice, the CP  
204 potential near the dielectric surface (particularly visible in Movie S1 as the constant potential around the dielectric structure)  
205 and GMs of the waveguide (only present in Movie S2). The black dots represent individually calculated atomic trajectories  
206 initialized in 5 separate pancakes and launched 60  $\mu\text{m}$  from the waveguide at time  $\tau = 0$  (time counter observed in upper left  
207 corner of the movies). The black dots become red a single frame before the trajectory intersects the boundary of the dielectric  
208 structure and are removed from the simulation. The lattice speed in free-space is 0.51 m/s, lattice depth is 500  $\mu\text{K}$ , and initial  
209 temperature  $T = 150 \mu\text{K}$  for atoms trapped in the lattice. Note that the number of atoms is much larger per pancake for the  
210 movies (ie 20000 atoms per pancake) than the experiment ( $\simeq 500$  atoms per pancake) to illustrate the multitude of trajectories  
211 a single atom could potentially follow. The two gray rectangles are a cross section at the thick part of the APCW, as indicated  
212 by the red dashed line in Fig. 2(a).

213  
214 **Movie S1. Red lattice delivery of atoms with no Stark GMs.** This movie is of atomic trajectories using  
215 the conditions of Fig. 5(a) in the main text (no Stark GM). The four frames in Fig. 5(a) are generated  
216 using a single pancake of atoms from this simulation movie. The link to the movie can be found here:  
217 <https://dx.doi.org/10.14291/vd6s-6h38>

218 **Movie S2. Red lattice delivery with blue detuned TM Stark GM.** This movie portrays the conditions of Fig.  
219 5(d) in the main text (in the presence of a TM Stark GM). Here, the blue detuned TM Stark GM repels  
220 atoms from the dielectric surfaces and imposes position and time dependent AC-Stark shifts. As before, the  
221 four frames in Fig. 5(d) indicate the evolution of a single pancake taken from this simulation movie. The link  
222 to the movie can be found here: <https://dx.doi.org/10.14291/r6xg-j678>

223 **References**

- 224 1. Metcalf HJ, Van der Straten P (2012) *Laser cooling and trapping*. (Springer Science & Business Media).
- 225 2. Hood JD, et al. (2016) Atom–atom interactions around the band edge of a photonic crystal waveguide. *Proc. Natl. Acad. Sci. U.S.A.* 113(38):10507–10512.
- 226 3. Asenjo-Garcia A, Hood JD, Chang DE, Kimble HJ (2017) Atom-light interactions in quasi-one-dimensional nanostructures: A Green’s-function perspective. *Phys. Rev. A* 95(3):033818–16.
- 227 4. Goban A, et al. (2015) Superradiance for atoms trapped along a photonic crystal waveguide. *Phys. Rev. Lett.* 115(6):063601.
- 228 5. COMSOL (2017) COMSOL Multiphysics Reference Manual, version 5.3 ([www.comsol.com](http://www.comsol.com)).
- 229 6. Johnson SG, Joannopoulos JD (2001) Block-iterative frequency-domain methods for maxwell’s equations in a planewave basis. *Opt. Express* 8(3):173–190.
- 230 7. Intravaia F, Henkel C, Antezza M (2011) Fluctuation-induced forces between atoms and surfaces: The casimir–polder interaction in *Casimir Physics*. (Springer), pp. 345–391.
- 231 8. Grimm R, Weidemüller M, Ovchinnikov YB (2000) Optical dipole traps for neutral atoms in *Advances in atomic, molecular, and optical physics*. (Elsevier) Vol. 42, pp. 95–170.
- 232 9. Hindmarsh AC, et al. (2005) SUNDIALS: Suite of nonlinear and differential/algebraic equation solvers. *ACM Transactions on Mathematical Software (TOMS)* 31(3):363–396.
- 233 10. Fuchs S, Bennett R, Krems RV, Buhmann SY (2018) Nonadditivity of optical and casimir-polder potentials. *Phys. Rev. Lett.* 121(8):083603.
- 234 11. Fuchs S, Bennett R, Buhmann SY (2018) Casimir-polder potential of a driven atom. *Phys. Rev. A* 98(2):022514.
- 235 12. Chang DE, Jiang L, Gorshkov A, Kimble H (2012) Cavity qed with atomic mirrors. *New J. Phys.* 14(6):063003.
- 236 13. Lin Yj, Teper I, Chin C, Vuletić V (2004) Impact of the casimir-polder potential and johnson noise on bose-einstein condensate stability near surfaces. *Phys. Rev. Lett.* 92(5):050404.
- 237 14. McGuirk JM, Harber DM, Obrecht JM, Cornell EA (2004) Alkali-metal adsorbate polarization on conducting and insulating surfaces probed with bose-einstein condensates. *Phys. Rev. A* 69(6):062905.
- 238 15. Hung C, Meenehan S, Chang D, Painter O, Kimble H (2013) Trapped atoms in one-dimensional photonic crystals. *New J. Phys.* 15(8):083026.
- 239 16. Yu SP, et al. (2014) Nanowire photonic crystal waveguides for single-atom trapping and strong light-matter interactions. *Appl. Phys. Lett.* 104(11):111103.
- 240 17. Bannerman ST, Price GN, Viering K, Raizen MG (2009) Single-photon cooling at the limit of trap dynamics: Maxwell’s demon near maximum efficiency. *New J. Phys.* 11(6):063044.